ARTICLE

Rational Screening of Single-Atom-Doped ZnO Catalysts for Propane Dehydrogenation from Microkinetic Analysis

-Received 00th January 20xx,
Accepted 00th January 20xx

DOI: 10.1039/x0xx00000x

Fang Ma,[a, §] Qing-Yu Chang,[a, §] Qiang Yin,[a] Zhi-Jun Sui,[a] Xing-Gui Zhou,[a] De Chen,[b] Yi-An Zhu[a,*]

Supported single-atom catalysts, which bridge the gap between homogeneous and heterogeneous catalysis, have attained increasing interest because of their unique catalytic properties and behaviors. In this contribution, periodic DFT+U calculations have been carried out to explore the structural stability, catalytic activity, and selectivity of 13 M_1-ZnO (M = Mn - Cu, Ru - Ag, and Os - Au) catalysts in propane dehydrogenation (PDH). Calculated results indicate that the doped single atoms show high resistance to sintering on the ZnO surface. Except on Rh_1-, Os_1-, Ir_1-, and Pt_1-ZnO($10\bar{1}0$), a Lewis acid-base interaction occurs, which would greatly enhance the coadsorption of a pair of amphoteric species on the oxides. The linear chemisorption energy and transition state energy scaling relations hold well for the C-H and H-H bond activation steps involved in the reaction network. Microkinetic analysis is used to determine the activity trend and volcano-shaped plots of the turnover frequency for propylene production are obtained, with the formation energies of adsorbed H and 2-propyl used as two reactivity descriptors. By using the activation energy difference between propylene dehydrogenation and desorption as a measure of the catalyst selectivity, it is found that a high selectivity can only be achieved at the expense of catalytic activity. Comparison between the energy barriers for H_2 desorption and H_2O formation indicates that the reduction of ZnO can be suppressed by single-atom doping. The Mn- and Cu-doped ZnO catalysts are suggested to be good catalyst candidates for PDH with lower cost, increased activity, and improved selectivity and catalytic stability.

1. Introduction

Propylene is an important building block for the production of a wide variety of chemicals, such as polypropylene, propylene oxide, acrylonitrile, and so on.[1] The conventional way to produce propylene is via steam cracking and fluidized catalytic cracking, which can no longer meet the ever increasing demand for propylene. Recently, particular interest has been focused on propane dehydrogenation (PDH) because the large-scale exploration of shale gas provides an exciting opportunity for producing light olefins from relatively cheap alkanes.[2] As PDH is a strongly endothermic process, it requires to be catalyzed at high reaction temperatures, which results in a major challenge due to coke formation.[3] Cr- and Pt-based catalysts have long been used in the commercial processes for the catalytic dehydrogenation of alkanes. However, chromium oxides suffer from fast deactivation, and the environmental concerns associated with the toxicity of the Cr species have limited its further commercial applications.[4-6] The Pt-based catalysts exhibit good activity for the dehydrogenation reaction,[7, 8] but the selectivity towards propylene and catalyst stability are still unsatisfactory.[9-11] Hence, there has been a considerable increase in the research activity driven by the desire to develop new and more effective catalyst for PDH.

Experimentally, various transition-metal oxides such as Ga_2O_3,[12, 13] V_2O_5,[14-16] ZnO,[17] ZrO_2,[18, 19] and TiO_2[20] have been studied in catalyzing PDH, among which zinc oxide is one of the most promising candidates. It was reported that small ZnO nanoclusters may act as the active phase,[21] showing high initial catalytic activity for C-H bond cleavage. However, the ZnO catalyst deactivates very quickly as a result of poisoning of the active sites by coke deposition.[22] In addition, in the reducing atmosphere, the decomposition of zinc oxide clusters (and hence the formation of metallic zinc) may readily occur, leading to a poor structural and catalytic stability.[23, 24] The loss of the reactivity requires that the catalyst be regenerated frequently, thus increasing the complexity of the process.

ZnO has been extensively studied in a great many of catalytic reactions, such as methanol synthesis,[25] methanol partial oxidation,[26] methanol steam reforming,[27, 28] the water-gas shift reaction,[29] and the dehydrogenation of light alkanes.[17, 30] To inhibit deactivation and improve the catalytic performance for a specific reaction, synthesis of composite oxides and modification of ZnO have been proposed. For instance, a series of Zn-Nb-O oxides via the co-precipitation method were synthesized by Sun et al,[22] which show higher activity and stability in the catalytic dehydrogenation of propane to propylene. As another example, Liu et al.[17] prepared ZnO/Al_2O_3 and Pt-modified ZnO/Al_2O_3 catalysts by using an impregnation method. It was found that the introduction of only 0.1 wt% Pt can dramatically improve the catalytic activity and suppress the reduction of ZnO. Detailed characterization of the catalyst structures indicated that Pt is highly dispersed on the catalyst surface and Pt crystallites cannot be detected, so the improved catalytic performance was attributed to the electronic

[a] UNILAB, State Key Laboratory of Chemical Engineering, School of Chemical Engineering, East China University of Science and Technology, Shanghai 200237, China. E-mail: yanzhu@ecust.edu.cn
[b] Department of Chemical Engineering, Norwegian University of Science and Technology, N-7491 Trondheim, Norway
§ These authors contributed equally to this work
† Electronic Supplementary Information (ESI) available.

interactions between Pt and ZnO. In addition, after 4h of the PDH reaction, no metallic zinc was observed on the spent 15Zn0.1Pt catalyst and the amount of H_2O generated is also much lower than that on the corresponding 15Zn catalyst.

Single-atom catalysis is an area of intense current research. On the one hand, single-atom catalysts exhibit properties that are distinctly different from those of supported nanoclusters and nanoparticles.[31-38] On the other hand, single-atom catalysts have well-defined local structures and therefore provide an opportunity for establishing the structure-reactivity relationship. The rational fabrication of model catalytic materials depends crucially on an understanding of this link. Apart from the work by Liu et al.[17], Gu et al. dispersed single Pt atom onto ZnO($10\bar{1}0$) to catalyze methanol steam reforming. By combining experimental with theoretical results, they suggested that the observed increase in the activity is due to the stronger bonding between single Pt sites and the reactants/intermediates.[27] Rawal et al. also found that, in the methanol partial oxidation reaction, Pd_1-ZnO showed remarkable and excellent catalytic performance compared to $Pd_{16}Zn_{16}$ and pristine ZnO($10\bar{1}0$), where they attributed the increased activity to the great influence of the singly dispersed Pd atom on the local environment of the active Zn sites.[26] Despite a great deal of research, it is still not clear how the doped single atoms would modify the electronic structure of the ZnO surface and how the two components actually function in the chemical reactions. More importantly, there are no rules based on simple physical properties that can be used to guide us in predicting the trend in the activity of the single-atom-doped ZnO catalysts.

In this work, DFT+U calculations and microkinetic analysis have been carried out to explore the catalytic behavior of 13 M_1-ZnO (M = Mn, Fe, Co, Ni, Cu, Ru, Rh, Pd, Ag, Os, Ir, Pt, and Au) catalysts in PDH. The geometry and thermal stability of M_1-ZnO are first studied. Then, the preferred adsorption site and adsorption energies of reaction intermediates have been discussed. Next, the Lewis acid-base interaction is examined on the ZnO($10\bar{1}0$) and M_1-ZnO($10\bar{1}0$) surfaces by energy decomposition and electronic structure analysis. After that, linear scaling relations are established to identify the descriptor that can be used to describe the reaction kinetics. Finally, we conclude by discussing the implication of our results for rational design of single-atom-doped ZnO catalysts for PDH.

2. Computational details

2.1 DFT Calculation

All plane-wave DFT calculations were carried out using the VASP package.[39] The Bayesian error estimation functional with van der Waals correlation (BEEF-vdW)[40] was used to treat the exchange and correlation in the Kohn-Sham theory, and the interactions between ion cores and valence electrons were represented by the project-augmented wave (PAW) method.[41] By using the "hard" PAW potentials with valence configurations of Zn ($3d^{10}4s^2$), Mn_{pv} ($3p^63d^54s^2$), Fe_{pv} ($3p^63d^64s^2$), Co ($3d^74s^2$), Ni_{pv} ($3p^63d^84s^2$), Cu ($3d^94s^2$), Ru_{pv} ($4p^64d^75s^1$), Rh_{pv} ($4p^64d^85s^1$), Pd ($4d^{10}$), Ag ($4d^{10}5s^1$), Os ($5d^66s^2$), Ir ($5d^76s^2$), Pt ($5d^96s^1$), and Au ($5d^{10}6s^1$), a plane-wave energy cutoff of up to 600 eV was found to be necessary to converge the total energy per atom to within 1 meV. Because standard exchange-correlation functional suffers from excessive electron delocalization which is connected with the spurious interaction of an electron with itself (known as the "self-interaction error"), an additional Hubbard-type term was applied in a simplified DFT+U method.[42-44] The effective U for Zn in ZnO (U_{eff} = 4.1 eV) was obtained by fitting thermodynamic properties to available experimental data, in much the same way as that proposed by Li et al.[45] The reason that the Hubbard-type term was not used to localize the strongly correlated d electrons in the other transition metals is given in Sec. S1 in the Supporting Information. Brillouin zone sampling was performed using the Monkhorst-Pack method and the partial occupancies of the valence bands were determined by the Gaussian method with an energy smearing of 0.1 eV. Spin-polarized calculations were performed to obtain reasonably accurate structures and energetics of the transition-metal oxides.

2.2 Structural model

The optimized lattice constants of bulk ZnO are a = 3.244 Å and c = 5.219 Å, which agree satisfactorily with the experimentally measured values (a = 3.249 Å and c = 5.210 Å). A four-unit-layer slab with a $p(2 \times 2)$ supercell was used to represent the ZnO($10\bar{1}0$) surface, and adjacent slabs were separated by a vacuum spacing of 12 Å along the surface normal. The two unit layers of the ZnO ($10\bar{1}0$) slab were keep fixed at their crystal lattice positions while the adsorbate and the reminder of the slab were allowed to fully relax. A $5 \times 3 \times 1$ Monkhorst-Pack k-point grid was used to sample the Brillouin zone of the supercells. Geometry optimization and transition-state search were conducted until the forces acting on each atom were below 0.05 eV / Å. The M_1-ZnO($10\bar{1}0$) (M = Mn, Fe, Co, Ni, Cu, Ru, Rh, Pd, Ag, Os, Ir, and Au) surfaces were constructed by substituting M for Zn. The geometries of the ZnO($10\bar{1}0$) and M_1-ZnO($10\bar{1}0$) surfaces are shown schematically in Fig. 1a and 1b, respectively. On ZnO($10\bar{1}0$), the Zn and O ions in the outermost unit layer can be divided into two groups each, depending on their connections and the topography of the surface. For example, the O ions that lie above and below the exposed Zn ions are denoted as O_1 and O_2, respectively. When the surface is doped with single transition-metal atoms, however, the outermost O ions adjacent to the M cation are no longer equivalent and an O_3 site is newly formed.

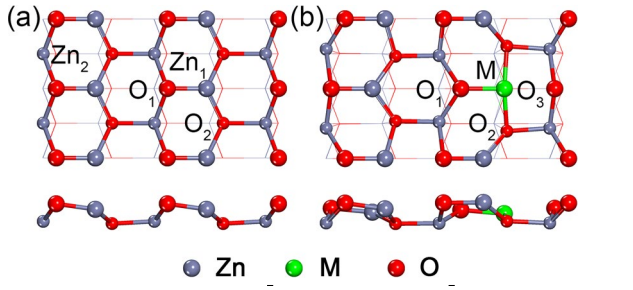

Fig. 1 Top and side views of (a) ZnO($10\bar{1}0$) and (b) M_1-ZnO($10\bar{1}0$).

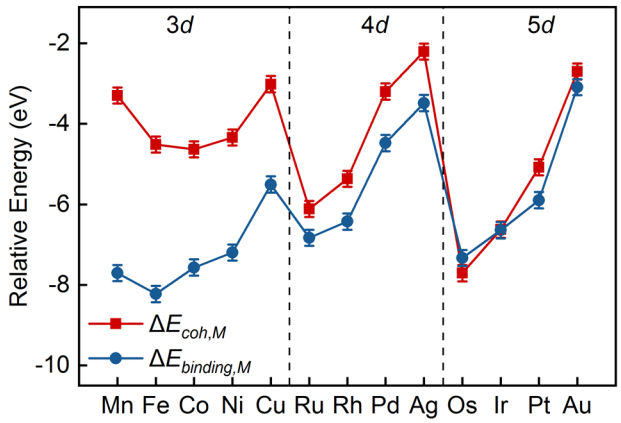

Fig. 2 Comparison between the binding energy of M to the Zn-deficient ZnO surface and the cohesive energy of bulk M.

2.2 Microkinetic Analysis

Microkinetic analysis was performed under typical PDH reaction conditions at 873.15 K and 1 bar of C_3H_8 by using the CatMAP code.[46] The TOFs for elementary steps were obtained by solving a mean-field model under the steady state approximation. The thermodynamic properties of gas-phase and surface-adsorbed species were calculated in the ideal-gas and harmonic limits, respectively, and the details have been given in our previous work.[47] The rate-determining step was identified by calculating the degree of rate control based on the method proposed by Campbell et al.[48, 49]:

$$X_{ij} = \frac{d\log(r_i)}{d\left(-G_j / k_B T\right)} \quad (1)$$

where X_{ij}, r_i, G_j, k_B, and T represent the degree of the rate control matrix, the rate of production of product i, the Gibbs free energy of species j, Boltzmann's constant, and the absolute temperature, respectively.

3. Results and discussion

3.1 Geometry and structural stability of M_1-ZnO

It is well known that the main obstacle with respect to the commercialization of single-atom catalysts is given by the thermal degradation of active metal phase. A strong metal-support interaction plays a key role in preventing sintering of single atoms on the surface.[50, 51] High-angle annular dark-field (HAADF) experiments indicated that isolated single atoms can be anchored onto ZnO($10\bar{1}0$) by replacing Zn, and the calculated formation energies of Pt- and Au-doped ZnO showed that the embedded Pt and Au are thermodynamically stable and resistant to sintering during the course of catalyst synthesis and catalytic reactions.[27] Our previous DFT calculations also demonstrated that substitution of Pt for Zn is energetically more favorable than substitution of Pt for O and adsorption of Pt on the oxide surface.[52]

To assess the structural stability of all the M_1-ZnO($10\bar{1}0$) surfaces of interest, the binding energy ($\Delta E_{binding,M}$) of a single atom to the Zn-deficient surface and the cohesive energy ($\Delta E_{coh,M}$) of bulk M are calculated as

$$\Delta E_{binding,M} = E_{M_1-ZnO} - E_{defective} - E_{atom,M} \quad (2)$$

and

$$\Delta E_{coh,M} = E_{bulk,M} - E_{atom,M} \quad (3)$$

respectively, where E_{M_1-ZnO}, $E_{defective}$, $E_{atom,M}$, and $E_{bulk,M}$ are the total energies of the M_1-ZnO($10\bar{1}0$) surface, the Zn-deficient ZnO surface, an isolated M atom, and an atom in the bulk of metallic M. The difference between these two quantities provides a measure of how readily the single atoms can aggregate to form a metal cluster. The calculated $\Delta E_{binding,M}$ and $\Delta E_{coh,M}$ are presented in Fig. 2. From the figure, one can see that, with the exception of Os and Ir, most transition-metal atoms have a more negative binding energy than the cohesive energy. Given the uncertainty of DFT calculations (~0.2 eV), all the single atoms of interest can stay atomically dispersed on the defective ZnO surface. Furthermore, we have gradually increased the surface coverage of the doped atoms and found that there exists a maximum possible value of 1/4 ML, beyond which a stable M_1-ZnO($10\bar{1}0$) surface structure can no longer be retained. This finding, on the other hand, demonstrates that the use of a large $p(2 \times 2)$ supercell is essential to the calculations in this work. The details can be found in Sec. S2 in the Supporting Information.

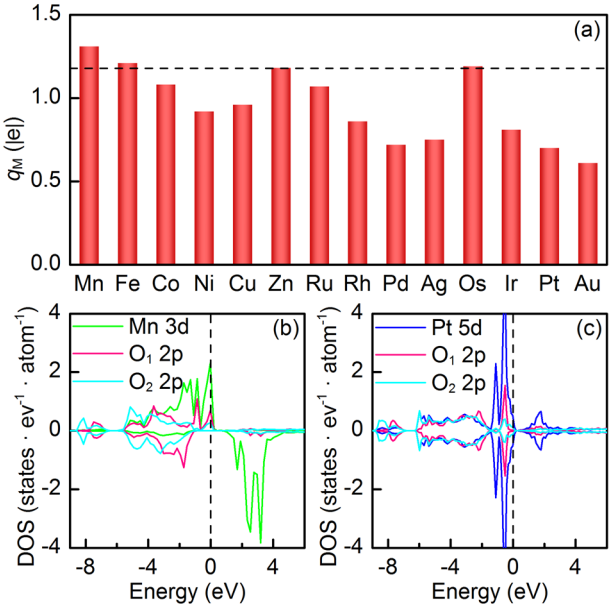

Fig. 3 (a) Calculated effective Bader charges on single atoms and calculated DOSs projected onto the d orbital of the single atom and the p orbital of oxygen on (b) Mn_1-ZnO and (c) Pt_1-ZnO.

3.2 Electronic structure of M_1-ZnO($10\bar{1}0$)

Then, the Bader charge analysis was performed to explore the nature of the interaction between M_1 and the defective ZnO. As indicated in Fig. 3a, all the metal ions have positive charges, indicating that there is a flow of electrons from the single atoms to the surface. In addition, the oxidation states of the single atoms including Zn itself are much less positive than the formal oxidation state of Zn in ZnO, implying that the chemical bonding is ionic with some covalent character. Most single

atoms, except Mn, Fe, and Os, carry less positive charges than Zn on the pristine surface, causing the surfaces to be electron-deficient. Hence, the presence of the single atoms must have a pronounced effect on the adsorption and catalytic properties of their adjacent O ions.

In addition, substitution of other transition metals for Zn makes the slab model non-stoichiometric and electrically charged. It seems that charge compensation is required to achieve electrostatic stabilization of the charged atomic layers. Hence, to see if it is important to make such compensations, we calculated the binding energy of M_1 and the oxygen vacancy formation energy after creating Zn vacancy on the rear side of the slab of Mn_1-ZnO($10\bar{1}0$) and adsorbing H on Pt_1-ZnO($10\bar{1}0$), where Mn and Pt are high- and low-valence dopants, respectively. The calculated results indicate that compensating for charges has a negligible or even negative effect on the structural stability of the doped surfaces, making the aggregation of single atoms to form islands and creation of oxygen vacancy thermodynamically more favorable. The details are given in Sec. S3 in the Supporting Information.

In light of the information given by the Bader charge analysis, density of states (PDOSs) projected onto the metal d orbital and its neighboring O 2p orbitals are calculated on Mn_1-ZnO and Pt_1-ZnO, as shown in Fig. 3b and 3c, respectively. From the figure, one can see that the overlap between either the Mn 3d or Pt 5d orbitals and the O_1 2p is significant above and below the Fermi level, suggesting a very strong interaction between them. On the other hand, the Mn 3d orbital only weakly mixes with the O_2 2p orbital compared to the interaction between the Pt 5d and the O_2 2p orbitals. This observation is also reflected in the measured the M-O bond length. On Mn_1-ZnO, the Mn-O_1 and Mn-O_2 bond lengths differ greatly (1.905 Å vs. 2.019 Å), while on Pt_1-ZnO the Pt-O_1 and Pt-O_2 bonds are 2.029 and 2.009 Å in length, respectively, which compare closely to each other.

3.3 Adsorption properties of M_1-ZnO

According to our previous work,[53, 54] the adsorption of propane and propylene on the catalyst surfaces plays a major role in describing the kinetics of PDH. The activation of physisorbed propane, namely, the initial C-H bond breaking, is often the rate-determining step that governs the rate law for the overall dehydrogenation reaction, and the activation energy difference between propylene dehydrogenation and desorption can be used as a measure of the catalyst selectivity toward propylene production.

The adsorption energy of simple species on the M_1-ZnO surfaces was calculated as

$$\Delta E_{ads} = E_{surface+adsorbate} - E_{surface} - E_{adsorbate} \quad (4)$$

where $E_{surface+adsorbate}$, $E_{surface}$, and $E_{adsorbate}$ are the total energies of the surface with species adsorbed, bare surface, and free gas-phase species, respectively. Under this definition, a negative value of the ΔE_{ads} indicates an energy-gain process. A more negative ΔE_{ads} value is an indication of a stronger adsorbate-substrate interaction.

The calculated adsorption energies and the optimized adsorption configurations are summarized in Table S4 and Fig. S4, respectively. Upon geometry optimization, propane and H_2 are adsorbed on the M_1-ZnO surfaces without forming a chemical bond, which is reflected in the calculated small adsorption heats that fall within the typical range of weak physisorption. Unlike propane and H_2, propylene prefers to adsorb on top of the single atoms in the π adsorption mode, except on Mn_1-ZnO where its physisorption is found to be energetically more favourable. Actually, it was reported that the physisorption of propylene on the pristine ZnO is also thermodynamically favoured, although the corresponding chemisorption energy could be negative.[52] The explanation is that the surface and propylene are greatly distorted upon chemisorption, giving rise to highly positive distortion energies and hence a small chemisorption heat.

As the final state for the first dehydrogenation step in PDH, adsorbed 2-propyl and H were found to be the rate-limiting intermediates on the ZnO($10\bar{1}0$) surface.[52] The overall rate of the reaction can be increased by stabilizing their adsorption. On the single-atom-doped surfaces, 2-propyl and H are adsorbed preferentially at either the M or the O_3 site. In our previous study[52], it was observed that the H at the Zn_1 site accepts a certain number of electrons donated by a second H that is bound to the next-nearest neighbor O_3 site. As a consequence, the sum of the adsorption energies of the individually adsorbed H atoms is significantly less negative than when they are coadsorbed.

Historically, Lewis acidity and basicity can have various definitions and classifications,[55] but it is generally accepted that when two species are brought into contact, the one that withdraws electrons is the Lewis acid and the one that donates electrons is the Lewis base. The observed enhancement of the bonding upon H coadsorption can therefore be explained by the Lewis acid-base interaction proposed by Meitu et al.,[56] where the H at the O site acts as the Lewis base and the H at the M site as the Lewis acid.

Apart from the Zn_1 and O_3 ion pair, four additional Zn-O sites are first selected to study the coadsorption of H and H (H&H) on ZnO($10\bar{1}0$), as shown schematically in Fig. 4a. Upon optimization, it is found that Zn_1-O_1 and Zn_1-O_3 are the only two sites that can accommodate the coadsorbed H atoms. The two H atoms initially placed at the Zn_2 and O_1 ion pair would be relaxed to the adjacent Zn_1-O_3 site. At the Zn_1-O_2 and Zn_2-O_2 sites, the coadsorbed H and H cannot form covalent bonds to the surface. The energetically most favorable site for H&H adsorption is the Zn_1-O_1 site, and the coadsorption energy is calculated to be -5.03 eV, 0.25 eV more negative than that at the Zn_1-O_3 site. Here the coadsorption energy is defined as

$$\Delta E_{co-ads} = E_{surf+acid+base} - E_{surf} - E_{acid} - E_{base} \quad (5)$$

where $E_{surf+acid+base}$, E_{surf}, E_{acid}, and E_{base} are the total energies of the oxide surface with the acid and base coadsorbed, the bare surface, gas-phase acid and base, respectively. In addition, the calculated adsorption energies of two coadsorbed H atoms at these two sites are more negative than the sum of the adsorption energies of individually adsorbed H atoms, as can be seen in Table S5. To measure the strength of the direct interaction between the Lewis acid and Lewis base, the coadsorption energy of H and H is rewritten as

$$\Delta E_{co-ads} = \Delta E_{ads,acid}^{constrained} + \Delta E_{ads,base}^{constrained} - \Delta E_{distortion,surf} + \Delta E_{int,acid-base} \quad (6)$$

where $\Delta E_{ads,acid}^{constrained}$ and $\Delta E_{ads,base}^{constrained}$ are the adsorption energies of the acid and base with the geometries constrained to those upon coadsorption, and $\Delta E_{distortion,surf}$ is calculated as the energy difference of the oxide surface before and after coadsorption. Under this definition, $\Delta E_{int,acid-base}$ is a measure of the Lewis acid-base interaction on the metal oxides and a positive value gives an indication of the absence of Lewis acid-base interaction. The details of the derivation of the equations are included in the Supporting Information.

The contributions to the adsorption energy of H&H on ZnO($10\bar{1}0$) is summarized in Table S5. It can be seen that the $\Delta E_{int,acid-base}$ has a negative value at both the Zn_1-O_1 and the Zn_1-O_3 sites. Interestingly, although the length of the Zn_1-O_3 bond (3.313 Å) is about 1.077 Å longer than that of the Zn_1-O_1 bond, the $\Delta E_{int,acid-base}$ at the Zn_1-O_3 site is more negative, meaning that a stronger Lewis acid-base interaction can occur even if the distance between Zn and O is greater.

To examine more closely the nature of the chemical bonds on the pristine surface, the effective Bader charge and charge density difference are computed at the Zn_1-O_1 and Zn_1-O_3 sites to keep track of the charge redistribution upon coadsorption of two H atoms. The calculated effective Bader charges are listed in Table S5 and the charge density difference for H adsorption at the O sites is computed with another H atom pre-adsorbed at the adjacent Zn_1 site, as shown in Fig. 4b and 4c. The calculated results indicate that the H at the O sites has the almost same number of positive charges, regardless of whether the Zn_1 site is occupied. By comparison, upon coadsorption a certain number of electrons are transferred from the H at the O sites to that at the Zn_1 site through the oxide surface. Moreover, the H at the Zn_1 ion carries more negative charge when the other H is coadsorbed at the O_3 site than at the O_1 site. Hence, the reason for the stronger Lewis acid-base interaction at the Zn_1-O_3 site is that the H adsorption at the O_3 site can more dramatically enhance the ability of the surface to donate electrons to the Zn_1 ion.

Because it has been recognized that the interaction between a Lewis acid and a Lewis base coadsorbed at the Zn_1-O_3 site could be surprisingly strong and has a pronounced effect on the adsorption property of the metal oxide, coadsorption of H and H as well as 2-propyl and H is also studied by positioning them at the corresponding M-O_3 site where strong Lewis acid-base interactions are likely to take place. The calculated adsorption energies of 2-propyl, 2-propyl&H, and H&H are summarized in Table S4, where 2-propyl&H refers to the coadsorption of 2-propyl and H. Like on the ZnO surface, the coadsorption energies of two H atoms at the corresponding M-O_3 site on the M_1-ZnO($10\bar{1}0$) surfaces are found to be more negative than the sum of the adsorption energies of individually adsorbed H atoms, except for Ru_1-ZnO, Ag_1-ZnO, Ir_1-ZnO, and Au_1-ZnO where coadsorption would weaken the bonding between the H atoms and the surface (see Table S6). Here we also decomposed the coadsorption energy of H&H on the M_1-ZnO surfaces to examine how the Lewis acid-base interaction may affect the coadsorption behaviors of the different single-atom-doped surfaces, and the calculated energy components are shown in Fig. 5a. From the figure, it is clear that, with the exception of Rh_1-ZnO, Os_1-ZnO, Ir_1-ZnO, and Pt_1-ZnO, most of the doped surfaces give rise to a negative $\Delta E_{int,acid-base}$ upon coadsorption of a pair of amphoteric species, implying the presence of a strong Lewis acid-base interaction. Surprisingly, the binding of the coadsorbed H to the surface could be weakened even if a strong Lewis acid-base interaction occurs, as is the case for the coadsorption on Ag_1-ZnO. Conversely, the attachment can be enhanced on the surfaces where the Lewis acid-base interaction does not occur, as is the case for the coadsorption on Pt_1-ZnO. Hence, the reason that the adsorption energy difference and $\Delta E_{int,acid-base}$ do not follow the same trend can be traced to the fact that sometimes adsorbate and substrate are distorted to different degrees in the presence and absence of the coadsorbed species and the distortion energies differ greatly.

To shed light on the electron density redistribution upon coadsorption of reaction intermediates on the M_1-ZnO($10\bar{1}0$) surfaces, Bader's analysis was performed and the calculated values are listed in Table S6. Furthermore, since Mn_1-ZnO($10\bar{1}0$) and Pt_1-ZnO($10\bar{1}0$) are two representative surfaces where the Lewis acid-base interaction occurs and does not occur, respectively, the charge density difference for coadsorption of two H atoms on these two surfaces are also illustrated in Fig. 5b and 5c. For the other doped surfaces, the flow of electrons is shown schematically in Fig. S5 in the Supporting Information. The calculated results indicate the charge on the H atom at the O_3 site does not change regardless of whether an acid is adsorbed at the Mn or Pt site. By comparison, when a second H sits at the next-nearest neighbor O site, the adsorbed H at the Mn site gains 0.20 electrons.

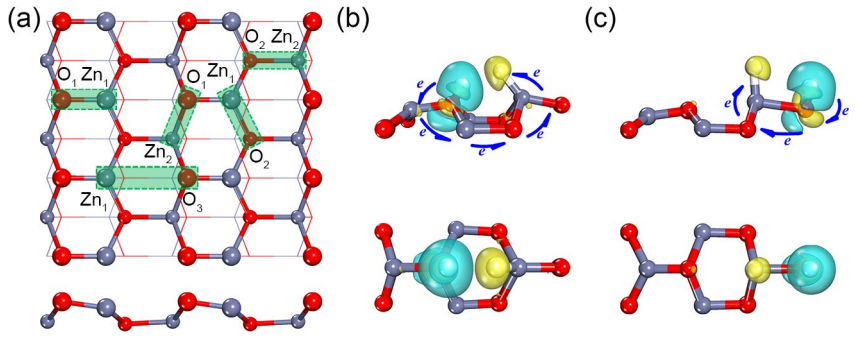

Fig. 4 (a) Top and side views of the zinc and oxygen ion pairs on the ZnO($10\bar{1}0$) surface; side and top views of the computed charge density difference for coadsorption of H&H at the (b) Zn_1-O_3 and (c) Zn_1-O_1 sites. Charge accumulation and depletion are colored yellow and cyan, respectively, with the isosurface value being 0.02 e/Å^3

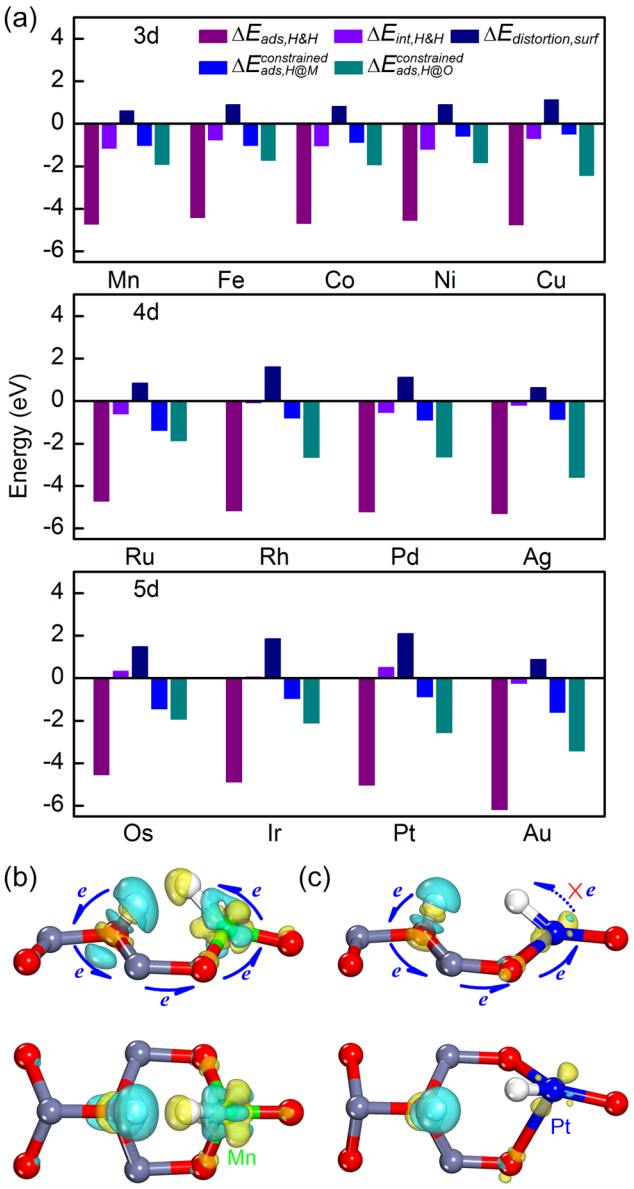

Fig. 5 (a) Decomposition of the coadsorption energy of two H atoms on the M_1-ZnO surfaces; side and top views of the computed charge density difference for coadsorption of H&H on (b) Mn_1-ZnO and (c) Pt_1-ZnO. Charge accumulation and depletion are colored yellow and cyan, respectively, with the isosurface value being 0.05 e/Å^3.

However, the charge on the H atoms adsorbed at the Pt remains nearly constant before and after coadsorption. Therefore, the strong Lewis acid-base interaction occurs if the presence of a Lewis base at the O site may enhance the ability of the oxide surface to donate electrons to the Lewis acid, which in turn gives rise to a stronger chemical bonding between the adsorbate and the surface.

3.4 Energetics of Propane Dehydrogenation

It is generally accepted that the main reaction of PDH occurs by successive removal of two H atoms from the methyl and methylene groups in propane, followed by desorption of propylene and H_2 from the catalyst surface. Fig. 6a and 6b illustrates the geometries of the initial, transition, and final states for the first and second dehydrogenation steps on Mn_1-ZnO($10\bar{1}0$) and Pt_1-ZnO($10\bar{1}0$), respectively. One reason the M-O_3 site is under consideration is that in a first test the Zn_1-O_3 site can accelerate the first dehydrogenation step by an activation energy of 1.07 eV, which is slightly lower than that at the Zn_1-O_1 site (see Fig. S6). Another reason is that, in a previous study[52], the Pt-O_3 site proved to be much more active than the Zn_1-O_3 site for the scission of C-H bonds in propane to form propylene, indicating that the M-O_3 site would dominate the activity for the dehydrogenation reaction, at least on certain single-atom-doped ZnO surfaces.

As can be seen in Fig. 6a and 6b, on Mn_1-ZnO($10\bar{1}0$) and Pt_1-ZnO($10\bar{1}0$), the transition states for the first dehydrogenation step are quite similar in geometry, where one of the C-H bonds on the methylene group is effectively destroyed and the detaching H atom sits at the O_3 site, leaving the 2-propyl group bonded to the M site via a carbon-to-metal σ bond. The only difference is that the activated C-H bond on Pt_1-ZnO($10\bar{1}0$) is stretched more dramatically because of the larger atomic size of Pt. More importantly, on both the two surfaces, the transition state closely resembles the corresponding final state (namely, the coadsorbed 2-propyl and H), giving an indication of late transition states.

As for the second dehydrogenation step, the situation is quite different. On Mn_1-ZnO($10\bar{1}0$) the activated complex is final-state like; that is, it has a geometry similar to the coadsorbed propylene and H. On Pt_1-ZnO($10\bar{1}0$), however, the transition state is close to the initial state (the chemisorbed 2-propyl) on the potential energy surface because in the final state the propylene molecule is physisorbed on the oxide surface without forming a chemical bond, giving rise to a completely different electronic structure from that of the transition state. Thus, according to the transition state geometry for the dehydrogenation of 2-propyl, the pristine and single-atom-doped ZnO($10\bar{1}0$) surfaces fall into two categories. The first group consists of Mn_1-ZnO, Fe_1-ZnO, Co_1-ZnO, Ni_1-ZnO, Cu_1-ZnO, Ru_1-ZnO, Rh_1-ZnO, Ag_1-ZnO, and Au_1-ZnO. The second group contains ZnO, Pd_1-ZnO, Os_1-ZnO, Ir_1-ZnO, and Pt_1-ZnO. It is important to note that the difference in the structural resemblance does not bear any direct relation to whether or not the Lewis acid-base interaction is present. Actually, we will see later that the two groups differ greatly in the transition state energy scaling relation for the second dehydrogenation step.

The Gibbs free energy diagrams for PDH over the two groups of the ZnO-based surfaces are shown in Fig. 6c and 6d, where the detached H is assumed to have no effect on the kinetics because H migration into bulk ZnO was believed to readily take place.[57] From the figure, it can be seen that the diagrams on Fe_1-ZnO and ZnO are quite uphill but, in each category, as the adsorbed species are bound more tightly to the surfaces, the diagrams become more and more neutral. For the dehydrogenation reactions where bond cleavage occurs, the transition state energy is lowered more dramatically than that of the initial state, leading to a lowered activation energy. The explanation is that the transition state has a more extended geometry and would therefore be stabilized to a larger extent.[58]

It has been suggested by Andersson et al.[59] that the point with the highest energy in the Gibbs free energy diagrams usually defines the slowest reaction step. Thus, one can see that

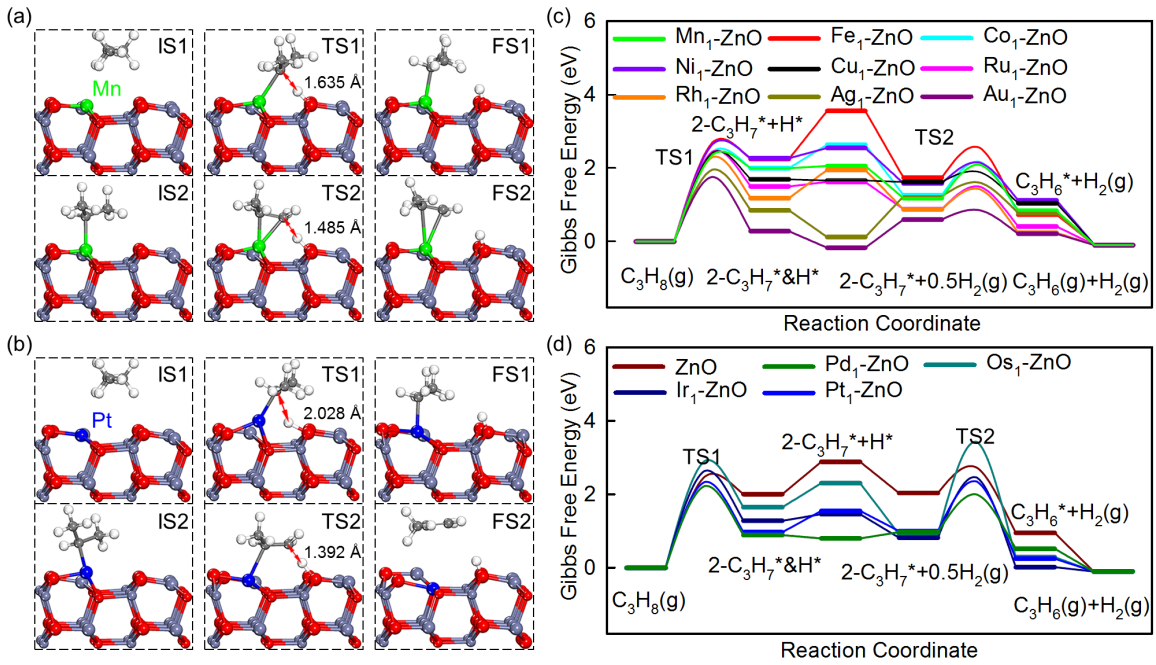

Fig. 6 Geometries of the initial, transition, and final states for the first and second dehydrogenation steps on (a) Mn_1-ZnO($10\bar{1}0$) and (b) Pt_1-ZnO($10\bar{1}0$); (c, d) Gibbs free energy diagrams for PDH on pristine and single-atom-doped ZnO($10\bar{1}0$) at 873.15 K and 1 bar of C_3H_8. All the Gibbs free energies are calculated relative to the sum of the Gibbs free energies of gas-phase propane and bare oxide surface.

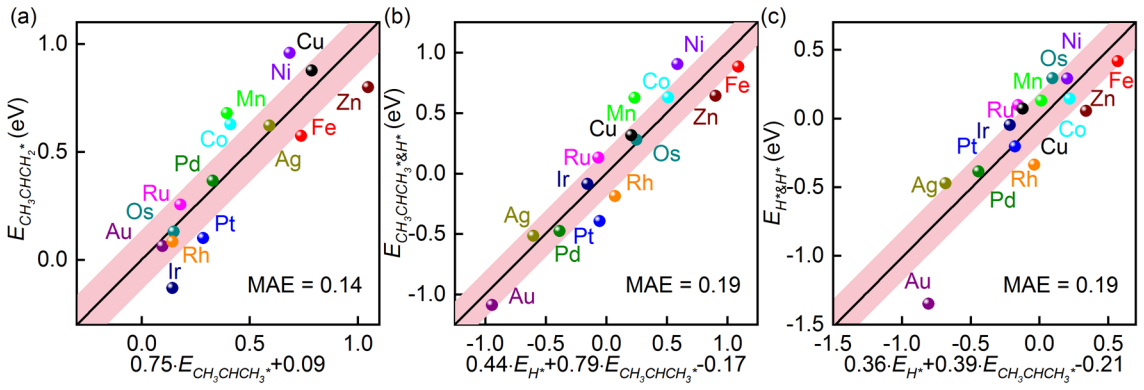

Fig. 7 Calculated formation energies of (a) propylene, (b) 2-propyl&H, and (c) H&H as a function of the formation energies of adsorbed H at the O site and adsorbed 2-propyl at the M site. The formation energies of the species are calculated in the same way as that suggested in earlier studies.[61, 62]

the overall rate on the ZnO-based catalysts is generally controlled by a TOF-determining transition state that is for either the first or the second dehydrogenation step. Exceptions occur on Fe_1-ZnO and ZnO where the kinetics is governed by a TOF-determining intermediate, namely, the individually adsorbed 2-propyl and H, as has been demonstrated in a previous microkinetic analysis study.[52] In addition, it is interesting to find that the Au-, Ag-, and Cu-doped ZnO catalysts show a strong activity toward C-H bond activation, although these transition metals in their elemental form are very inactive for C-H bond activation. The explanation is that Au, Ag, and Cu which have *d* orbitals fully occupied in the metallic state become positively charged upon doping [see Fig. 3(a)], and the resulting metal cations and oxygen ions interact strongly with the carbon-containing species and H, respectively, as can be seen in Table S4. On the other hand, according to the Sabatier principle, the best catalyst should have a moderate binding ability. If adsorption is too weak, reactants cannot be adsorbed on the surface, while if adsorption is too strong, then the reaction suffers from the poisoning of the catalyst surface and from the undesired side reactions (in our case, deep dehydrogenation). Hence, although the Gibbs free energy diagram is a useful tool that may provide an overview of the kinetics for a given reaction, detailed microkinetic analysis is highly desired to achieve a clear picture.

3.5 Linear scaling relations

The rational design of modern catalytic materials depends crucially on a quantitative understanding of the detailed reaction mechanism. However, there is a considerable increase in mathematical complexity as soon as the reaction mechanism has more than a couple of elementary steps. Many of the rate

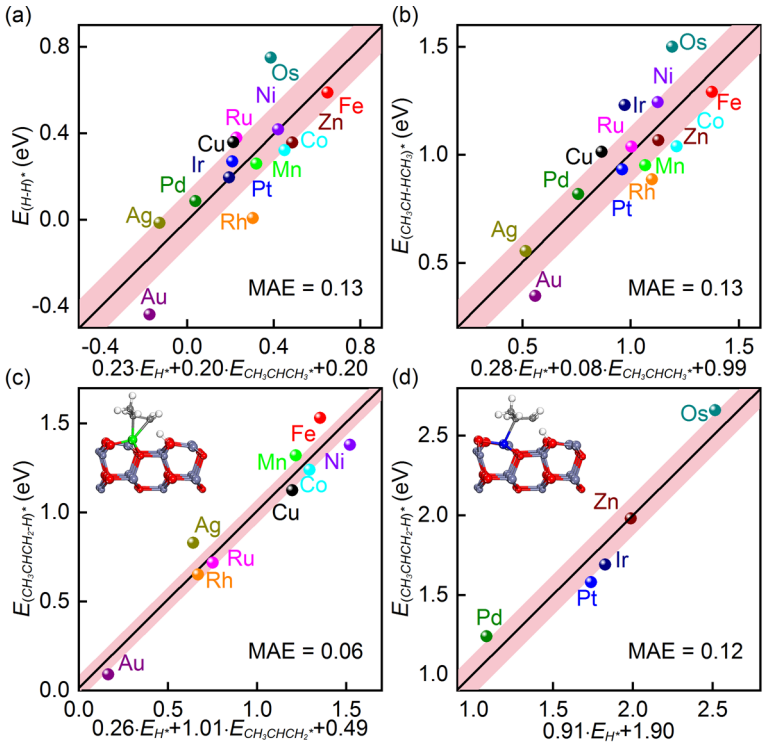

Fig. 8 Calculated formation energies of the transition states for (a) hydrogen recombination and (b) dehydrogenation of propane, and (c, d) dehydrogenation of 2-propyl as a function of the formation energies of adsorbed H at the O site and adsorbed 2-propyl at the M site (adsorbed propylene at the M site).

laws are so complicated that their solutions cannot be cast as functions. One approach is to integrate the differential equations numerically, but in this way we cannot recognize the pattern of the activity over a class of catalyst surfaces and often get lost in details.

Scaling relations are found to be of extraordinary power in identifying descriptor(s) that describes the kinetics of a chemical reaction. These relations are based on the fact that the chemisorption energies of reaction intermediates that are bonded to the surface via the same adsorbate and surface atom(s) scale with each other.[60] Unlike on transition-metal surfaces, H binds very strongly to the O site on the metal oxides and its bonding to the surface often dominates the interaction between the coadsorbed species and the substrate, as can be sees in Table S4. In addition, the structural analysis above clearly indicates that the transition states for the dehydrogenation steps resemble either the adsorbed 2-propyl or the adsorbed propylene. Hence, the formation energies of adsorbed H and 2-propyl (or propylene) can probably be used as descriptors that explain the trends in the catalytic activity of the ZnO-based catalysts for PDH. The formation energy approach used in this work was proposed by Medford et al.[61], where the energy of each species is computed by using a "reference state" for each element present in the gas-phase and adsorbed species involved in the reaction. One advantage of this approach is that it does not distinguish between adsorbate states and transition states and their formation energies can be calculated relative to the same set of "atomic reference energies". Because it ensures thermodynamic consistency, the use of formation energies as inputs to a kinetic model is preferred over other relative quantities such as adsorption, reaction, and activation energies. Here the total energies of free H_2 and C_3H_8 were used to calculate the "atomic reference energies" of H and C, and the energy of the species in the surface is referenced to that of the bare slab. The details of the derivation of the formation energies are given in Sec. S11 in the Supporting Information.

Fig. 7 shows the calculated formation energies of propylene, 2-propyl&H, and H&H as a function of the formation energies of H and 2-propyl. A two-variable linear regression analysis has been performed by making a least-squares fit of the data to the best straight line. It is important to note that, to avoid unphysical scaling (e.g., a very large positive regression for one variable and a very large negative coefficient for the other), the fitting is constrained so that only positive coefficients are allowed. As a consequence, in some cases, there is only one descriptor used to describe how strongly the adsorbate is bound to the surface. It is clear from the figure that very good linear scaling relations are established, implying that the formation energies of H and 2-propyl can be used to give a reasonably accurate estimate of the energies of other C3 and coadsorbed species. We have also tried many other single quantities and their combinations, but these two descriptors give the best fitting. As can be seen in Fig. S7, they do not scale with each other and are independent variables, which can be explained by the fact that H and 2-propyl are adsorbed at the oxygen and metal sites, respectively, and their interactions with the oxide surfaces differ greatly in nature.

Because the transition state energy can be envisioned as the chemisorption energy of the activated complex, it is reasonable

to expect that the transition state energy scaling relations hold for the dehydrogenation reactions. Indeed, plotting the formation energy of the transition states for hydrogen recombination and for the C-H bond breaking in propane against those of H and 2-propyl may give straight lines, as shown in Fig. 8a and 8b. As for the second dehydrogenation step, given the fact that the transition states on the first and second groups of the doped surfaces closely resemble the final and initial state, respectively, the transition state energies should be correlated to different combinations of descriptors. For the first group, the formation energy of the activated complexes increases linearly with those of H and propylene, as can be seen in Fig. 8c. Previously, the binding strengths of propyl and propylene to transition metals were found vary in much the same way.[11] It is therefore interesting to find that a similar transition state energy scaling relation can also be established by using the formation energies of adsorbed H and 2-propyl as two descriptors (see Fig. S8), although the resulting regression coefficients are distinctively different from those on the oxide surfaces of the second group (see Fig. 8d). Thus, the formation energies of adsorbed H and 2-propyl are capable of measuring the binding strength of all the reaction intermediates and activated complexes and can therefore be used as descriptors to describe the kinetics of PDH over M_1-ZnO.

3.6 Kinetics of propane dehydrogenation over M_1-ZnO

3.6.1 Activity map for propane dehydrogenation

The concept of volcano curve provides a foundation for high-throughput catalyst screening by mapping the reaction rate to the parameter space and further to the descriptor space.[61] Having identified the descriptors of the reactivity of the M_1-ZnO catalysts, we are now in a position to construct the activity map for PDH. Here, according to the scaling relations established above, the TOFs for PDH on the first and second groups of the M_1-ZnO catalysts are plotted as a function of the formation energies of H and 2-propyl in two different patterns, as shown in Fig. 9a and 9b, respectively. The only difference between them is the transition state energy scaling relation for the second dehydrogenation step, as illustrated above.

It can be seen from the figure that the two-dimensional activity maps are apparently volcano-shaped plots, each of which shows a single maximum. Interestingly, despite having different values, the two maxima can be attained with the E_{H^*} and $E_{CH_3CHCH_3^*}$ both in the range -1.5 ~ -0.5 eV. In addition, it is demonstrated again that two activity descriptors are necessary, for they do not scale with each other and neither of them alone can well describe the energetics of the reaction. Closer examination of the activity maps reveals that most the single-atom-doped ZnO catalysts except Fe- and Os-doped ZnO exhibit higher activity than the pristine ZnO. At a given $E_{CH_3CHCH_3^*}$, the PDH rate first increases and then decreases with increasing the binding strength of H to the O site. For example, Mn_1-ZnO shows a stronger activity than both Co_1-ZnO and Ag_1-ZnO. When the H-O bond is weak, the Co_1-ZnO is inactive because of a high C-H bond activation energy. On the other hand, if the strength of the adsorbate-substrate interaction becomes too great, as is the case for H adsorption on Ag_1-ZnO, it is hard for C-H bonds to find an active site to be activated,

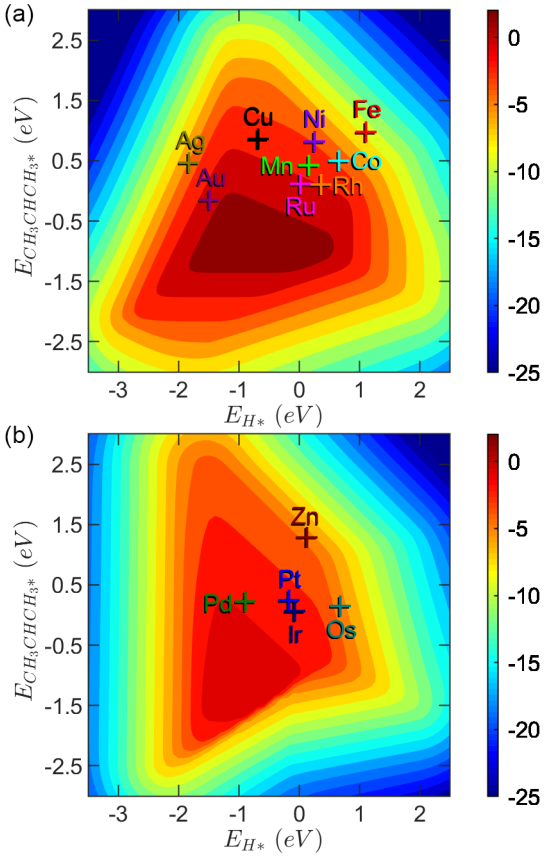

Fig. 9 TOFs for propane dehydrogenation to propylene as a function of the formation energies of adsorbed H at the O site and adsorbed 2-propyl at the M site on the (a) first and (b) second groups of the doped oxide surfaces.

thus giving rise to a low reaction rate.

Fig. 10 depicts the calculated coverages of H and free site on the single-atom-doped surfaces as a function of the two descriptors, and the data on the coverages of other reaction intermediates are included in Fig. S9 in the Supporting Information. From the figure, one can see that, on the Ag- and Au-doped ZnO surfaces, H is the most abundant surface species while on the other surfaces the vast majority of the active sites are unoccupied and ready for C-H bond breaking and H-H bond formation. As a result, on all the oxide surfaces concerned, the site coverages of other intermediates are negligibly small. In particular, H is too tightly bound to the O site on the Ag-doped surface, and its surface coverage approaches unity, which explains why the Ag_1-ZnO catalyst shows a poor catalytic activity for PDH although it has a relatively low activation energy for C-H bond activation.

Liu et al. reported that the upon addition of trace amount of Pt into ZnO, a lower degree of ZnO reduction and a higher catalytic activity have been observed.[17] In the present study, Au-, Ru-, Rh-, Pd-, Mn-, Cu-, and Ir-doped ZnO are predicted to be more active than Pt_1-ZnO for PDH. In particular, Au_1-ZnO is closest to the summit of the volcano and gives the highest catalytic activity, in accord with the prediction by the Gibbs free energy diagrams. The question that now arises is whether it also exhibits a high selectivity toward propylene production and a high structural stability in the reducing atmosphere.

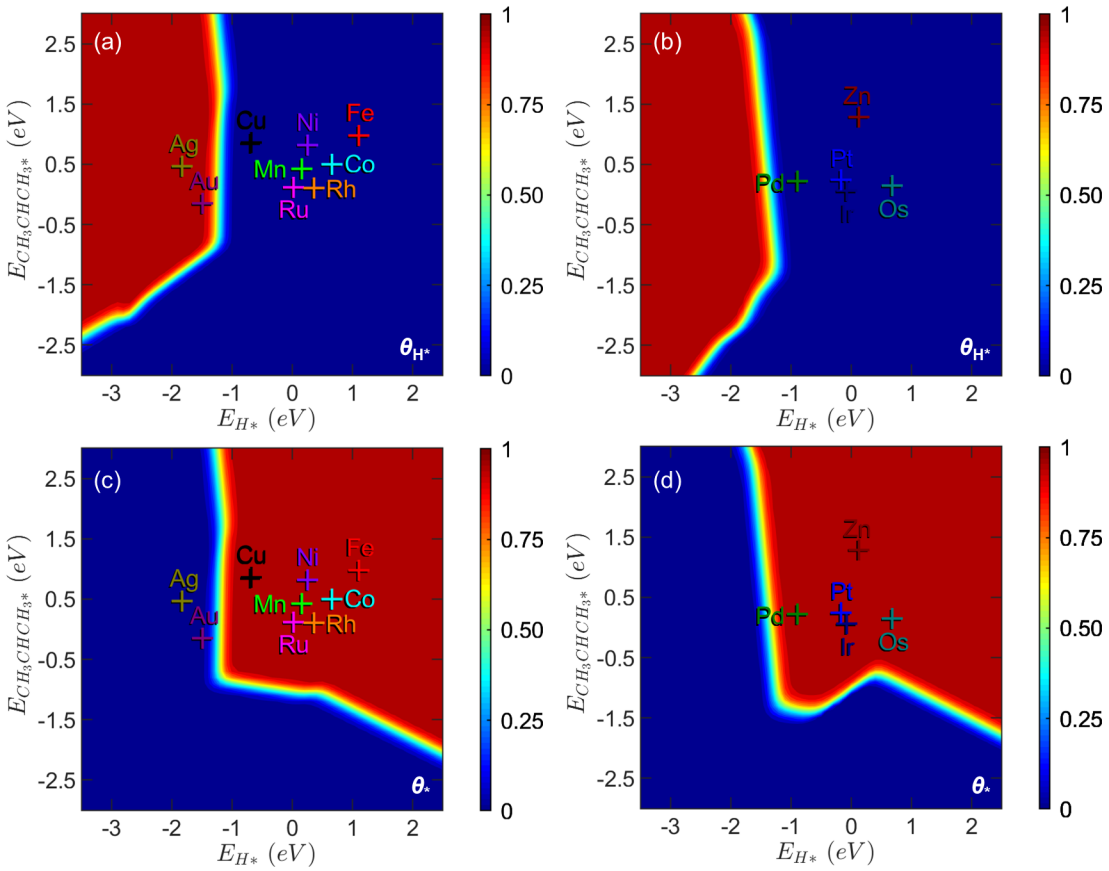

Fig. 10 Coverages of (a, b) H and (c, d) free site as a function of the formation energies of adsorbed H at the O site and adsorbed 2-propyl at the M site.

3.6.2 Selectivity toward propylene

In PDH, the deep dehydrogenation of propylene, followed by the cracking of the deeply dehydrogenated C3 species, has a negative effect on the catalyst selectivity and stability. Thus, detailed consideration of the competition between propylene dehydrogenation and desorption provides the key to understanding how the selectivity of ZnO can be tuned by single-atom doping. In principle, if the desorption barrier of propylene is lower than the activation energy for propylene deep dehydrogenation, propylene would be readily released from the oxide surface, leading to a good catalyst selectivity. Otherwise, deep dehydrogenation and cracking would take place, producing the precursors for coke deposition. Hence, in our previous work,[54] the activation energy difference between propylene dehydrogenation and desorption was proposed as a measure of the catalyst selectivity. The more positive the calculated value, the higher is the selectivity toward propylene, and hence the lower is the tendency for coke precursors to be formed.

Fig. 11a summarizes the calculated energy barrier differences over M_1-ZnO surfaces. A positive value gives an indication that desorption is kinetically favored. It can be seen that on ZnO($10\bar{1}0$) the energy barrier for deep dehydrogenation is 0.55 eV higher than that for propylene desorption. By comparison, on Au-, Ru-, Rh-, Ir, and Os-doped ZnO($10\bar{1}0$), the energy barrier for the deep dehydrogenation of propylene is lower than or nearly equal to that for propylene desorption, thereby leading to a low selectivity. In contrast, introduction of other transition metals may ensure that a high selectivity is attained. It is therefore clear that Au_1-ZnO, although very active for the C-H bond activation, suffers from the fast side reaction, and a high selectivity can only be achieved at the expense of a relatively low catalytic activity, as has also been observed in our previous work.[11] In this sense, the Pd_1-ZnO, Mn_1-ZnO, Cu_1-ZnO, and Pt_1-ZnO catalysts may stand out if a compromise is made between catalytic activity and selectivity. In particular, the remarkably good catalytic performance of Pt-doped ZnO for PDH has been demonstrated by Liu et al.[17].

3.7 Resistance to hydrogen reduction

Although transition-metal oxides have long been known to be active for C-H bond activation, one problem with their application in this type of reactions is the difficulty of stabilizing lattice oxygen and maintaining their crystal structures.[1] Therefore, it is of crucial importance to examine the structural stability of the doped ZnO catalyst in the reducing atmosphere. Here the activation energies for H_2 desorption and H_2O formation over the ZnO($10\bar{1}0$) and M_1-ZnO($10\bar{1}0$) surfaces are calculated and compared (shown in Fig. 11b and 11c), which can be used to measure how likely the ZnO-based catalysts can be reduced by the presence of H_2.

It can be seen from Fig. 11b that on ZnO($10\bar{1}0$) the energy barrier for the recombination of two H atoms at the Zn and O ion pair is 0.31 eV higher than that for H_2O formation, which means that H tends to escape with a surface O atom and go on

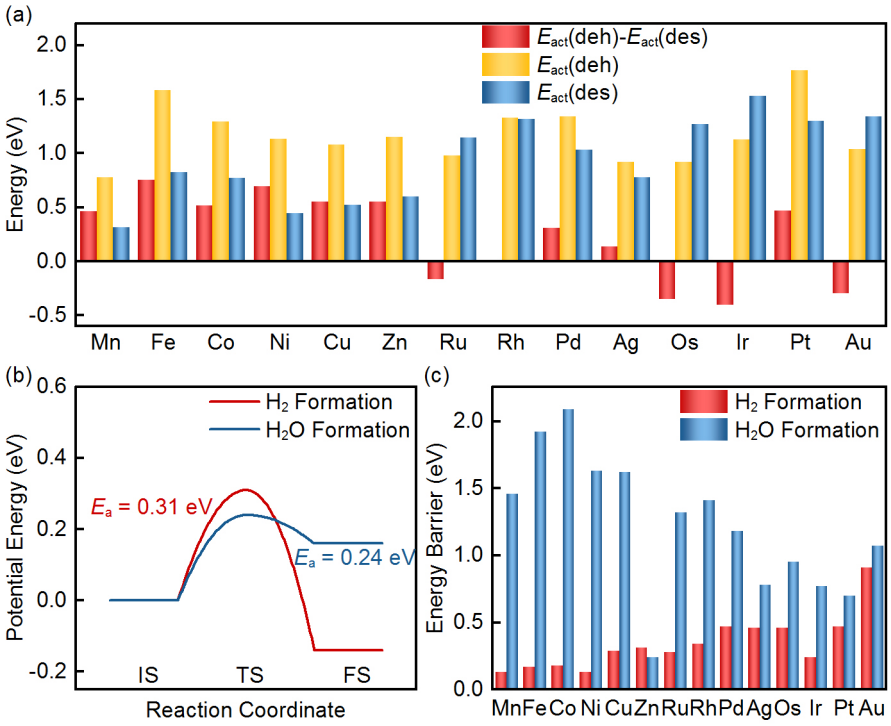

Fig. 11 (a) Energy barrier difference between propylene dehydrogenation and desorption on M_1-ZnO($10\bar{1}0$), (b) energy profiles and geometries of the transition states for H_2 desorption and H_2O formation on ZnO($10\bar{1}0$), and (c) comparison of the energy barriers for H_2 desorption and H_2O formation on M_1-ZnO($10\bar{1}0$)

to form H_2O, leaving the catalyst with oxygen vacancies and metal ions in lower oxidation states. This finding agrees well with the experimental observation that 20% Zn^{2+} is reduced to Zn^0 upon 4 hours of the PDH reaction.[17]

Upon doping the ZnO surface with single atoms (see Fig. 11c), the energy barriers for H_2O formation are invariably increased, and, more importantly, all of them are much higher than that for the corresponding H_2 desorption reaction, whichmeans that doping of single atoms on ZnO($10\bar{1}0$) may suppress ZnO reduction to some extent. Even for the smallest activation energy difference that occurs at the Au-O site, H_2 desorption takes place approximately 8 times faster than H_2O formation. Liu et al. also found that addition of trace amount of Pt into ZnO/Al_2O_3 could inhibit the reduction of the zinc oxide, although H_2O can still be detected in a lower amount.[17]

Since the single-atom-doped ZnO catalysts are surrounded mostly by the Zn-O sites, it is essential to compare the energy barriers at the Zn-O and M-O sites before using their difference to predict the resistance of the oxide catalysts to hydrogen reduction. One can see from the figure that among Pd_1-ZnO, Mn_1-ZnO, Cu_1-ZnO, and Pt_1-ZnO, the two noble-metal-doped catalysts prefer to activate the H-H and H-O bonds at the Zn-O site and, consequently, the structural stability remains unsatisfactory owing to the ready formation of oxygen vacancies. By contrast, Mn_1-ZnO and Cu_1-ZnO favor H_2 desorption at the M-O site, which is different from the theoretical predications by Chang et al.[62] who claimed that the Pt_1-Ga_2O_3 catalyst shows a bifunctional character in PDH where the Pt-O site brings about dehydrogenation while the Ga-O site is active for desorbing H_2. More importantly, Mn_1-ZnO is the sole catalyst that has a lower energy barrier for hydrogen recombination than for H_2O formation occurring at either the Zn-O or the M-O site and Cu_1-ZnO has the two activation energies comparable, both of which showing even better stability than Pt_1-ZnO in the reducing atmosphere. It can therefore be deduced that Mn_1-ZnO and Cu_1-ZnO are good non-precious catalyst candidates for PDH with improved catalyst selectivity and stability.

4 Conclusions

In this work, microkinetic analysis combined with results from DFT+U calculations has been performed to screen single-atom-doped ZnO catalysts for PDH, where 13 transition-metal elements including Mn, Fe, Co, Ni, Cu, Ru, Rh, Pd, Ag, Os, Ir, Pt, Au are substituted for surface Zn ions.

Our calculated results indicate that all the single atoms of interest can stay atomically dispersed on the defective ZnO surface and have a strong interaction with the surrounding O ions. Through energy decomposition and electronic structure analysis, it is found that a strong Lewis acid-base interaction occurs on most M_1-ZnO($10\bar{1}0$) except Rh_1-, Os_1-, Ir_1-, and Pt_1-ZnO, which can be traced to the fact that the adsorption of Lewis base may enhance the ability of the oxide surface to donate electrons to the Lewis acid. Very good linear scaling relations have been established, and the formation energies of adsorbed H and 2-propyl are identified as descriptors that can be used to give a reasonably accurate estimate of the energies of other adsorbed species and activated complexes.

By using descriptor-based microkinetic analysis, the turnover frequency for PDH over ZnO-based catalysts is plotted as a function of the two descriptors. Two volcano-shaped plots are

given based on the different transition state energy scaling relations for the second dehydrogenation step, where the optimal catalyst can be found with both the descriptors in the range -1.5 ~ -0.5 eV. The Pd_1-ZnO, Mn_1-ZnO, Cu_1-ZnO, and Pt_1-ZnO catalysts may stand out if a compromise is made between catalytic activity and selectivity. Doping of single atoms on ZnO($10\bar{1}0$) may suppress ZnO reduction in the reducing atmosphere. In particular, Mn_1-ZnO and Cu_1-ZnO can act as good non-precious catalysts for PDH with improved catalyst selectivity and stability. These theoretical results provide new guidelines for the rational design of non-precious transition-metal oxide catalysts for PDH.

ASSOCIATED CONTENT

Supporting information

Calculated adsorption energies of propylene before and after U_{eff} applied to doped single atoms on Mn_1-ZnO and Cu_1-ZnO, binding energies of Pt to Zn-deficient ZnO($10\bar{1}0$) at various Pt coverages, charge compensation on Pt_1-ZnO and Mn_1-ZnO, calculated adsorption energies of reaction intermediates on single-atom-doped ZnO, adsorption configurations of reaction intermediates on M_1-ZnO, decomposition of H&H coadsorption energy at the Zn_1-O_1 and Zn_1-O_3 sites and effective Bader charge on adsorbed species on ZnO, decomposition of ΔE_{co-ads}, decomposition of H&H coadsorption energy and effective Bader charge on adsorbed species on M_1-ZnO, computed charge density difference for coadsorption of H&H on single-atom-doped surfaces, energy profiles for the 1st dehydrogenation step of propane on the pristine surface, formation energy approach, plot of the calculated formation energy of 2-propyl against the formation energy of H, calculated formation energy of the transition states for the dehydrogenation of 2-propyl as a functional of the formation energies of H and 2-propyl, and calculated coverages of reaction intermediates.

Conflicts of interest

There are no conflicts to declare.

Acknowledgements

This work is supported by the Natural Science Foundation of China (91645122, 21473053, and U1663221), the National Key Research and Development Program of China (2018YFB0604700), and the Fundamental Research Funds for the Central Universities (222201718003). The computational time provided by the Notur project is highly acknowledged.

References

1. J. J. H. B. Sattler, J. Ruiz-Martinez, E. Santillan-Jimenez and B. M. Weckhuysen, *Chem. Rev.*, 2014, **114**, 10613-10653.
2. P. C. A. Bruijnincx and B. M. Weckhuysen, *Angew. Chem. Int. Ed.*, 2013, **52**, 11980-11987.
3. J. Im and M. Choi, *ACS Catal.*, 2016, **6**, 2819-2826.
4. M. Santhosh Kumar, N. Hammer, M. Rønning, A. Holmen, D. Chen, J. C. Walmsley and G. Øye, *J. Catal*, 2009, **261**, 116-128.
5. V. Z. Fridman and R. Xing, *Ind. Eng. Chem. Res.*, 2017, **56**, 7937-7947.
6. X.-Q. Gao, W.-D. Lu, S.-Z. Hu, W.-C. Li and A.-H. Lu, *Chinese J Catal*, 2019, **40**, 184-191.
7. Y. Zhang, Y. Zhou, L. Huang, M. Xue and S. Zhang, *Ind. Eng. Chem. Res.*, 2011, **50**, 7896-7902.
8. L. Shi, G.-M. Deng, W.-C. Li, S. Miao, Q.-N. Wang, W.-P. Zhang and A.-H. Lu, *Angew. Chem. Int. Ed.*, 2015, **54**, 13994-13998.
9. L. Nykänen and K. Honkala, *ACS Catal.*, 2013, **3**, 3026-3030.
10. H.-Z. Wang, L.-L. Sun, Z.-J. Sui, Y.-A. Zhu, G.-H. Ye, D. Chen, X.-G. Zhou and W.-K. Yuan, *Ind. Eng. Chem. Res.*, 2018, **57**, 8647-8654.
11. L. Xiao, F. Ma, Y.-A. Zhu, Z.-J. Sui, J.-H. Zhou, X.-G. Zhou, D. Chen and W.-K. Yuan, *Chem. Eng. J.*, 2019, **377**, 120049.
12. J. J. H. B. Sattler, I. D. Gonzalez-Jimenez, L. Luo, B. A. Stears, A. Malek, D. G. Barton, B. A. Kilos, M. P. Kaminsky, T. W. G. M. Verhoeven, E. J. Koers, M. Baldus and B. M. Weckhuysen, *Angew. Chem. Int. Ed.*, 2014, **53**, 9251-9256.
13. Y. Xu, J. Chen, X. Yuan, Y. Zhang, J. Yu, H. Liu, M. Cao, X. Fan, H. Lin and Q. Zhang, *Ind. Eng. Chem. Res.*, 2018, **57**, 13087-13093.
14. S. A. Al-Ghamdi, M. M. Hossain and H. I. de Lasa, *Ind. Eng. Chem. Res.*, 2013, **52**, 5235-5244.
15. J. Long, Z. Zhao, T. Wu, C. Xiong, G. Sun, R. Mu and L. Zeng, *Angew. Chem. Int. Ed.*, 2018, **57**.
16. C. Xiong, S. Chen, P. Yang, S. Zha, Z.-J. Zhao and J. Gong, *ACS Catal.*, 2019, **9**, 5816-5827.
17. G. Liu, L. Zeng, Z.-J. Zhao, H. Tian, T. Wu and J. Gong, *ACS Catal.*, 2016, **6**, 2158-2162.
18. T. Otroshchenko, S. Sokolov, M. Stoyanova, V. Kondratenko, U. Rodemerck, D. Linke and E. Kondratenko, *Angew. Chem. Int. Ed.*, 2015, **54**.
19. T. Otroshchenko, V. A. Kondratenko, U. Rodemerck, D. Linke and E. V. Kondratenko, *J. Catal*, 2017, **348**, 282-290.
20. F. Jiang, L. Zeng, S. Li, G. Liu, S. Wang and J. Gong, *ACS Catal.*, 2015, **5**, 438-447.
21. C. Chen, Z. Hu, J. Ren, S. Zhang, Z. Wang and Z.-Y. Yuan, *ChemCatChem*, 2019, **11**, 868-877.
22. Y.-n. Sun, C. Gao, L. Tao, G. Wang, D. Han, C. Li and H. Shan, *Catal. Commun.*, 2014, **50**, 73-77.
23. J. A. Biscardi, G. D. Meitzner and E. Iglesia, *J. Catal*, 1998, **179**, 192-202.
24. S. M. T. Almutairi, B. Mezari, P. C. M. M. Magusin, E. A. Pidko and E. J. M. Hensen, *ACS Catal.*, 2012, **2**, 71-83.
25. M. Behrens, F. Studt, I. Kasatkin, S. Kühl, M. Hävecker, F. Abild-Pedersen, S. Zander, F. Girgsdies, P. Kurr, B.-L. Kniep, M. Tovar, R. W. Fischer, J. K. Nørskov and R. Schlögl, *Science*, 2012, **336**, 893.
26. T. Rawal, S. R. Acharya, S. Hong, D. Le, Y. Tang, F. Tao and T. S. Rahman, *ACS Catal.*, 2018, DOI: 10.1021/acscatal.7b04504.
27. X.-K. Gu, B. Qiao, C.-Q. Huang, W.-C. Ding, K. Sun, E. Zhan, T. Zhang, J. Liu and W.-X. Li, *ACS Catal.*, 2014, **4**, 3886-3890.
28. S.-S. Wang, H.-Y. Su, X.-K. Gu and W.-X. Li, *The Journal of Physical Chemistry C*, 2017, **121**, 21553-21559.

29. X. K. Gu, C. Q. Huang and W. X. Li, *Catal Sci Technol*, 2017, **7**, 4294-4301.
30. G. Wang, C. Li and H. Shan, *Catal Sci Technol*, 2016, **6**, 3128-3136.
31. A. Wang, J. Li and T. Zhang, *Nature Reviews Chemistry*, 2018, **2**, 65-81.
32. S. Mitchell, E. Vorobyeva and J. Perez-Ramirez, *Angew Chem Int Ed Engl*, 2018, DOI: 10.1002/anie.201806936.
33. X. Y. Sun, P. Han, B. Li and Z. Zhao, *J. Phys. Chem. C*, 2018, **122**, 1570-1576.
34. L. Zhang, L. Han, H. Liu, X. Liu and J. Luo, *Angew. Chem. Int. Ed.*, 2017, **56**, 13694-13698.
35. L. Han, X. Liu, J. Chen, R. Lin, H. Liu, F. Lü, S. Bak, Z. Liang, S. Zhao, E. Stavitski, J. Luo, R. R. Adzic and H. L. Xin, *Angew. Chem. Int. Ed.*, 2019, **58**, 2321-2325.
36. F. Lü, S. Zhao, R. Guo, J. He, X. Peng, H. Bao, J. Fu, L. Han, G. Qi, J. Luo, X. Tang and X. Liu, *Nano Energy*, 2019, **61**, 420-427.
37. H. Liu, X. Peng and X. Liu, *Chemelectrochem*, 2018, **5**, 2963-2974.
38. Y. Qiu, X. Peng, F. Lü, Y. Mi, L. Zhuo, J. Ren, X. Liu and J. Luo, *Chemistry – An Asian Journal*, 2019, **14**, 2770-2779.
39. G. G. Kresse and J. Furthmüller, *Comput. Mater. Sci.*, 1996, **54**, 11169.
40. J. Wellendorff, K. Lundgaard, A. Møgelhøj, V. Petzold, D. D. Landis, J. K. Nørskov, T. Bligaard and K. W. Jacobsen, *Phys. Rev.B*, 2012, **85**.
41. G. J. Kresse and D. Joubert, *Phys. Rev. B*, 1999, **59**, 1758.
42. V. Anisimov, J. Zaanen and O. Andersen, *Phys. Rev. B*, 1991, **44**, 943-954.
43. V. I. Anisimov, F. Aryasetiawan and A. I. Lichtenstein, *J. Phys.: Condens. Matter*, 1997, **9**, 767-808.
44. S. Dudarev, G. A. Botton, S. Y. Savrasov, C. Humphreys and A. P. Sutton, *Phys. Rev. B*, 1998, **57**, 1505-1509.
45. Y. Li, Y.-S. Zheng, Y.-A. Zhu, Z.-J. Sui, X. Zhou, D. Chen and W.-K. Yuan, *J. Phys.: Condens. Matter*, 2019, **31**.
46. A. Medford, C. Shi, M. Hoffmann, A. Lausche, S. R. Fitzgibbon, T. Bligaard and J. K. Nørskov, *Catal. Lett.*, 2015, **145**.
47. Y.-A. Zhu, D. Chen, X.-G. Zhou and W.-K. Yuan, *Catal. Today*, 2009, **148**, 260-267.
48. C. T. Campbell, *ACS Catal.*, 2017, **7**, 2770-2779.
49. C. Stegelmann, A. Andreasen and C. T. Campbell, *J. Am. Chem. Soc.*, 2009, **131**, 8077-8082.
50. Z.-K. Han and Y. Gao, *Chem. Eur.J.*, 2016, **22**, 2092-2099.
51. X.-F. Yang, A. Wang, B. Qiao, J. Li, J. Liu and T. Zhang, *Acc. Chem. Res.*, 2013, **46**, 1740-1748.
52. Q.-Y. Chang, Q. Yin, F. Ma, Y.-A. Zhu, Z.-J. Sui, X.-G. Zhou, D. Chen and W.-K. Yuan, *Ind. Eng. Chem. Res.*, 2019, **58**, 10199-10209.
53. M.-L. Yang, Y.-A. Zhu, X.-G. Zhou, Z.-J. Sui and D. Chen, *ACS Catal.*, 2012, **2**, 1247-1258.
54. M.-L. Yang, Y.-A. Zhu, C. Fan, Z.-J. Sui, D. Chen and X.-G. Zhou, *Phys. Chem. Chem. Phys.*, 2011, **13**, 3257-3267.
55. W. B. Jensen, *The Lewis acid-base concepts: an overview*, John Wiley & Sons, 1980.
56. H. Metiu, S. Chrétien, Z. Hu, B. Li and X. Sun, *The Journal of Physical Chemistry C*, 2012, **116**, 10439-10450.
57. W. H. Doh, P. Roy and C. Kim, *Langmuir : the ACS journal of surfaces and colloids*, 2010, **26**, 16278-16281.
58. J. K. Nørskov, T. Bligaard, B. Hvolbæk, F. Abild-Pedersen, I. Chorkendorff and C. H. Christensen, *Chem. Soc. Rev.*, 2008, **37**, 2163-2171.
59. M. P. Andersson, F. Abild-Pedersen, I. N. Remediakis, T. Bligaard, G. Jones, J. Engbæk, O. Lytken, S. Horch, J. H. Nielsen, J. Sehested, J. R. Rostrup-Nielsen, J. K. Nørskov and I. Chorkendorff, *J. Catal*, 2008, **255**, 6-19.
60. F. Abild-Pedersen, J. Greeley, F. Studt, J. Rossmeisl, T. Munter, P. Moses, E. Skúlason, T. Bligaard and J. Nørskov, *Phys Rev Lett*, 2007, **99**, 016105.
61. A. J. Medford, C. Shi, M. J. Hoffmann, A. C. Lausche, S. R. Fitzgibbon, T. Bligaard and J. K. Nørskov, *Catal. Lett.*, 2015, **145**, 794-807.
62. Q.-Y. Chang, K.-Q. Wang, P. Hu, Z.-J. Sui, X.-G. Zhou, D. Chen, W.-K. Yuan and Y.-A. Zhu, *AIChE J.*, 2020, DOI: 10.1002/aic.16232.